Fluidization of Micronic Particles in a Conical Fluidized Bed: Experimental and Numerical Study of Static Bed Height Effect

Alireza Bahramian
Dept. of Chemical Engineering, Hamedan University of Technology, P.O. Box, 65155 Hamedan, Iran

Martin Olazar
Dept. of Chemical Engineering, University of the Basque Country, P.O. Box, 644, 48080 Bilbao, Spain

DOI 10.1002/aic.12621
Published online May 2, 2011 in Wiley Online Library (wileyonlinelibrary.com).

The numerical simulations and experimental data of bed hydrodynamics in a conical fluidized bed unit are compared. Experimental studies have been carried out in a bed containing TiO_2 particles belonging to A/C boundary of Geldart's classification with a wide particle-size distribution. Thus, pressure measurements and an optical fiber technique allowed determining the effect of static bed height on the fluidization characteristics of micronic particles. Numerical simulations have then been performed to evaluate the sensitivity of gas-solids drag models. The Eulerian multiphase model has been used with different drag models and three boundary conditions (BC) consisting of no-slip, partial-slip, and free-slip. The numerical predictions using the Gidaspow drag model and partial-slip BC agreed reasonably well with the experimental bed pressure drop measurements. The simulation results obtained for bed expansion ratio show that the Gidaspow model with the free-slip BC best fit with the experimental data. © 2011 American Institute of Chemical Engineers *AIChE J,* 58: 730–744, 2012

Keywords: fluidization, hydrodynamics, CFD simulation, conical fluidized bed, drag models, boundary conditions

Introduction

Fluidization in conical vessels is a useful technique with a variety of applications in drying,[1–4] food processing,[5,6] pharmaceutical industry,[7–10] gasification and pyrolysis reactors,[11–14] and catalytic polymerization reactors.[15,16]

A conical fluidized bed is a hybrid gas-solid contacting system, and therefore shares the characteristics of both fluidized and spouted beds. The naming of these types of beds in the literatures is often informed by their geometrical shape and the ratio of bed inlet diameter to particle size.[3,17] This bed provides means for the good mixing and circulation for small solid particles with a wide size distribution. Therefore, knowledge on the hydrodynamics of gas and particle flow in conical fluidized bed is essential for their design at both lab-scale and in industrial applications.

Extensive research has been conduced on the fluidization behavior of classical powders in the 30 to 1000 μm size range[18] and, consequently, their behavior is relatively well understood.[19–22] Tanfara et al.,[23] studied the effect of fine particles beds with a wide size distribution on local voidage in a bench-scale conical fluidized bed. Their main conclusion is that fines form a monolayer around the relatively coarser particles and act as a lubricant, thus lowering the apparent bed viscosity. A lower apparent viscosity corresponded to smooth fluidization with fine bubbles. Geldart[19] argued that the effect observed could be explained by the reduction in mean particle diameter due to the addition of fines. Geldart's

Correspondence concerning this article should be addressed to A. Bahramian at bahramian@profs.hut.ac.ir.

© 2011 American Institute of Chemical Engineers

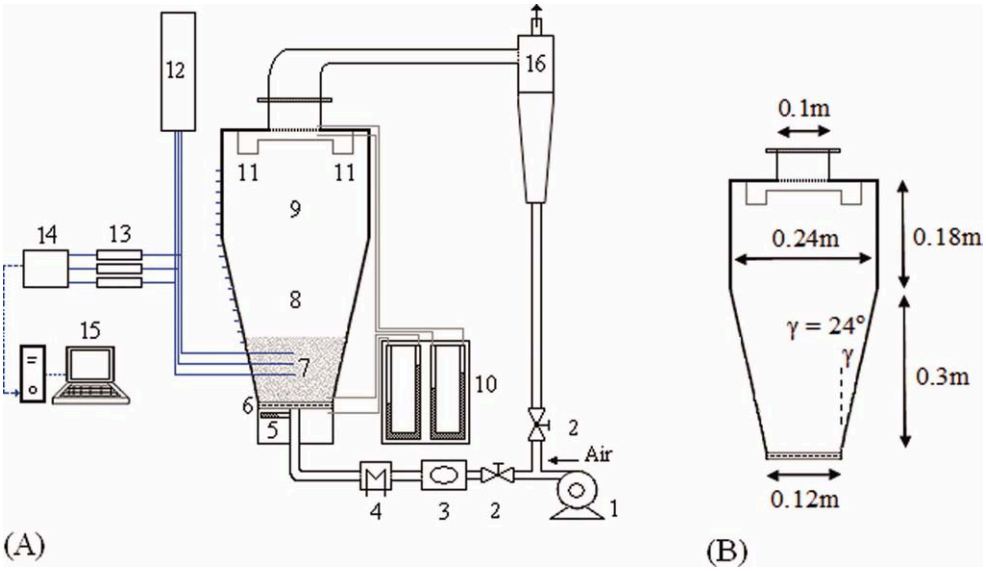

Figure 1. 1. Air compressor, 2. Valves, 3. Rotameter, 4. Electrical clement, 5. Probe thermometer, 6. Gas distributor, 7. Materials bed (TiO2 particles), 8. Conical section, 9. Cylindrical section, 10. Manometers, 11. Filters, 12. Light source, 13. Detectors, 14. Amplifier, 15. Computer and monitoring 16. Cyclone. (A) Experimental apparatus, (B) Dimensions of the bed.

[Color figure can be viewed in the online issue, which is available at wileyonlinelibrary.com.]

measurements for Geldart A powder revealed a definite influence of size distribution on bed hydrodynamics, such as increased bed expansion and decreased minimum fluidization velocity. Nevertheless, scant attention has been paid in the literature to the fluidization behavior of micro-size particles with wide size distribution in conical fluidized beds.

Experimental results[24–26] have shown that the solid flow in a spouted bed could be divided into three regions, namely, a spout zone in the center of the bed, an annulus between spout zone and the walls, and the fountain located at the expanded bed surface on top of the spout and annulus. The dynamic behavior of gas and particles in the spout zone has been predicted by Lefroy and Davidson[27] using a one-dimensional two-phase model. They show that the gas flow in the annular zone follows Darcy's law and that the pressure distribution at the interface between spout and annular zones follows a cosine function. Littman et al.,[28] use the vectorial form of the Eurgun equation[29] to predict gas and particles motion in a spout-fluid bed. Kwauk[30] reports that a decreasing fluid velocity gradient in the direction of fluid flow in a conical vessel has the following advantages: (1) A higher velocity at the lower section of the cone provides adequate fluidization of the coarse particles in a polydisperse particle bed, whereas a lower velocity at the top section prevents excessive carry-over of the fine particles. (2) The highly agitated coarse particles in the lower zone serve as normal gas distribution to disperse the fluidizing medium to the upper zone of the finer particles in the conical bed.

A considerable number of studies based on the progress made in numerical simulation techniques and computational fluid dynamics (CFD) have been published in recent years.[31–38] Huilin et al.,[39] incorporated a kinetic- frictional constitutive model for dense assemblies of solids in the simulation of spouted beds. Darelius et al.[40] applied a kinetic theory of granular flow and friction stress models using the slip and partial-slip boundary conditions (BC) for the solid-phase velocity at the wall, and their numerical results supported the experiments.

BC play an essential role in the CFD modeling of gas-solids systems for predicting the hydrodynamic behavior of fluidized beds. Benyahia et al.[36] used Jenkins BC in their simulations. They investigated two limits (low and high friction) in the solid phase for estimating the collision of solid particles with the wall, thereby predicting core-annulus flow. Their results show that a high friction BC causes unrealistically large granular energy production at the wall. Taghipour et al.,[41] and Almuttahar and Taghipour[38] applied boundary equations developed by Johnson and Jackson[42] in their simulation of a circulating fluidized bed riser. They report that the choice of different slip conditions, corresponding to free- or no-slip BC, affects the solid behavior of FCC particles near the riser wall.

This article experimentally and numerically studies the hydrodynamic behavior (especially pressure drop and bed expansion ratio) of poly-dispersed dried anatase TiO_2 particles in a conical fluidized bed for different gas velocities and static bed heights (particles loadings). The Eulerian two-phase CFD model is used to simulate the conical fluidized bed and the results obtained using three types of BC, i.e., no-slip, partial-slip, and free-slip are compared with the experimental data.

Apparatus and Experimental Set-up

The experiments have been carried out in a commercially available Plexiglas conical fluidized bed (STREA-1 from Aeromatic Ltd., Switzerland). This unit is geometrically similar to the industrial-scale one used in the petrochemical and pharmaceutical industries. The experimental apparatus and its dimensions are shown schematically in Figures 1A, B, respectively. There is a screen at the bottom of the conical fluidized bed (Standard wire mesh: 200), which acts as an

Table 1. The Size Distribution of TiO_2 Particles Used in this Work

Sieve Opening, d_{pi} (μm)	Weight fraction, x_i	$(x/dp)_i$	$d_{p,avg}$ (μm)
74 >	$1.64*10^{-2}$	$2.29*10^{-4}$	≈ 54
74–90	$1.60*10^{-2}$	$1.37*10^{-4}$	82
90–106	$8.96*10^{-2}$	$5.88*10^{-4}$	98
106–125	$2.92*10^{-2}$	$1.54*10^{-4}$	115
125–200	$2.70*10^{-1}$	$1.74*10^{-3}$	163
200–250	$1.47*10^{-1}$	$4.49*10^{-4}$	225
250–300	$1.14*10^{-1}$	$3.03*10^{-4}$	275
300–355	$5.64*10^{-2}$	$1.37*10^{-4}$	328
355–400	$2.49*10^{-1}$	$4.86*10^{-4}$	378
400–600	$1.24*10^{-2}$	$1.91*10^{-5}$	500
Total	1	$3.58*10^{-3}$	280

air distributor for preventing particle leakage from the bed when products with a high percentage of fine dust particles are treated.

The particles used throughout this experiment are dried anatase titanium dioxide (TiO_2) with diameters between 74 to 600 μm belonging to A/C boundary of Geldart's classification. Four different static bed heights, H_o, have been used, corresponding to 0.012, 0.024, 0.048, and 0.060 m (See Figure 1A).

The size distribution of the TiO_2 particles and their physical properties are given in Tables 1 and 2. The mean diameter (280 μm mean diameter) is used to determine the average particle size of the mixture.

Experiments have been performed to identify the steady-state bed pressure drop at different superficial gas velocities, U_g, from 0 to 1.5 m/s. Air (60 oC, 101,325 Pa) is used as fluidization medium and all the experiments have been carried out by increasing its flow rate from the fixed bed to fully fluidized state. The values of bed expanded have been obtained by using an optical fiber probe to determine the mean solid volume fraction at different axial positions. An r-z translator has been used to position the probe at the desired coordinative location. This device is provided with two stepper motors controlled through a GPIB port. More details on the experimental procedure are available elsewhere.[43–46]

Simulation Procedure and Boundary Conditions

An Eulerian-Eulerian multiphase model that includes granular kinetic theory and k-ε turbulence model has been used here for both the solid and gas phases to simulate the hydrodynamic behavior in a conical fluidized bed. The set of governing equations (see Appendix A) and k-ε turbulent model (see Appendix B) have been solved by the finite control volume technique. The two-dimensional axisymmetric segregated solver has been chosen in all the simulations.[47,48]

The pressure-velocity coupling has been achieved by using the phase coupled SIMPLEC algorithm. The velocities have been solved by coupling the two phases in a segregated state and the pressure equation was built based on total volume continuity rather than mass continuity. Pressure and velocities have been corrected to satisfy the continuity constraint. The mesh density in the computational domain is shown in Figure 2. The computational domain was discretized by 46,000 structured grid cells (as shown in Figure 2). This mesh has been chosen to fulfill the conditions for near-wall function and to minimize the solution's dependence on mesh density. A first-order upwind scheme and implicit formulation have been used to discretize the convection term.

The time step in unsteady simulations has been varied from 5×10^{-5} to 1×10^{-3} s, depending on the solution convergence. To minimize computation time, the time step automatically decreases when the solution changes rapidly and increases when fast transients subside. The computation time for simulating 5.5 s of real time is $\sim$22 h on a PC with a 3.2 GHz Pentium 4 CPU.

The assumptions and BC used in the simulations are as follows:

(1) Continuous phases were treated as ideal gas.

(2) The axisymmetric BC is applied along the axis of symmetry.

Table 2. Physical Properties of TiO_2 Particles

Property	Symbol (unit)	Value	
Average particle size	$d_{p,\ avg}$ (μm)	280	
Particle density	ρ_p (kg/m^3)	4500	
		H_o (m)	ρ_b (kg/m^3)
Bulk density	ρ_b (kg/m^3)	0.012	131
At different Static		0.024	133
Bed height, H_o		0.048	128
		0.060	125
Maximum packing limit	$\alpha_{s,max}$	0.67	

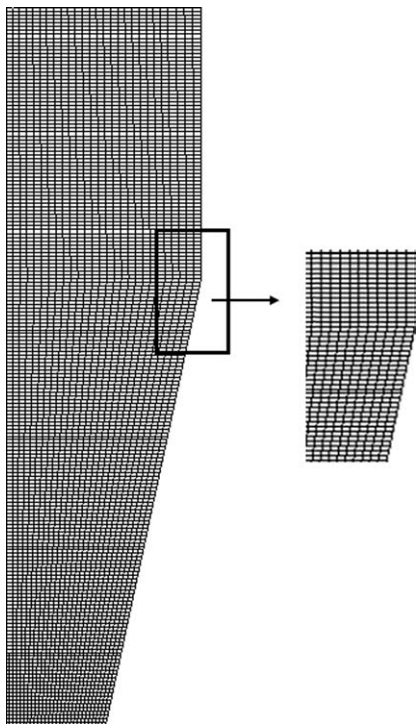

Figure 2. The computational mesh and the grid used for simulation.

Table 3. Simulation Performed at this Study

Simulation Runs	Friction	Slip Condition	Specularity Coefficient
1	Friction	No-slip	($\varphi = 1$)
2	Partial-friction	Partial-slip	($\varphi = 0.5$)
3	No-friction	Free-slip	($\varphi = 0$)

(3) At the entrance, the inlet gas velocity is assumed to be the linear gas velocity, U_g, (i.e., U_g = 0.1, 0.2, 0.3, 0.5, 0.7, 0.9, 1.19, and 1.43 m/s) and the inlet solid velocity is zero.

(4) At the outlet, an outflow BC is given, i.e., the velocity gradients for the two phases along the axial direction are zeros. Furthermore, pressure is also specified (atmospheric condition).

(5) At the wall, no-slip BC is used for the gas phase, whereas three types of slip coefficients are used for the solid phase. Based on this, Schaeffer[49] approach was used for no-slip condition, whereas semiempirical boundary equations developed by Johnson and Jackson[42] are applied for free- and partial-slip BC (Appendix C).

To assess the effect of BC on the model, runs have been carried out using three different BC for the solid phase, which are described in Table 3.

In the first simulation run (simulation run 1), the no-slip BC with frictional effect of particles on the wall is used. In the second one (simulation run 2), the partial-slip BC with a partial frictional effect of particles on the wall is used and, finally, in the third one (simulation run 3), the free-slip BC without frictional effect of particles on the wall is studied. Given that, the zero specularity coefficients cannot be applied mathematically to calculate the slip coefficient, an equivalent zero shear condition at the wall is applied to obtain the free-slip BC.

Results and Discussion

Experimental runs have been performed in a conical fluidized bed unit to identify the steady-state pressure drop, minimum fluidization velocity and bed expansion ratio (H/H_o), at different superficial gas velocities and four static bed heights, i.e., 0.012, 0.024, 0.048, and 0.060 m.

In all the runs, a bed containing poly-dispersed dried TiO_2 particles was fluidized at a superficial gas velocity, corresponding to the minimum fluidization velocity (U_{mf}), and the particles are entrained by the gas through the central core of the vessel (spout zone) and form a fountain at its top. The particles then descend by gravity and gas passing through the region between the wall and the spout (annular zone). The particle motion in the spout, annular and fountain zones leads to bed circulation. Similar particle flow patterns have already been reported in the literature for other gas-solid contact systems.[2,10,46] Jung and Gidaspow[50] found that the volume

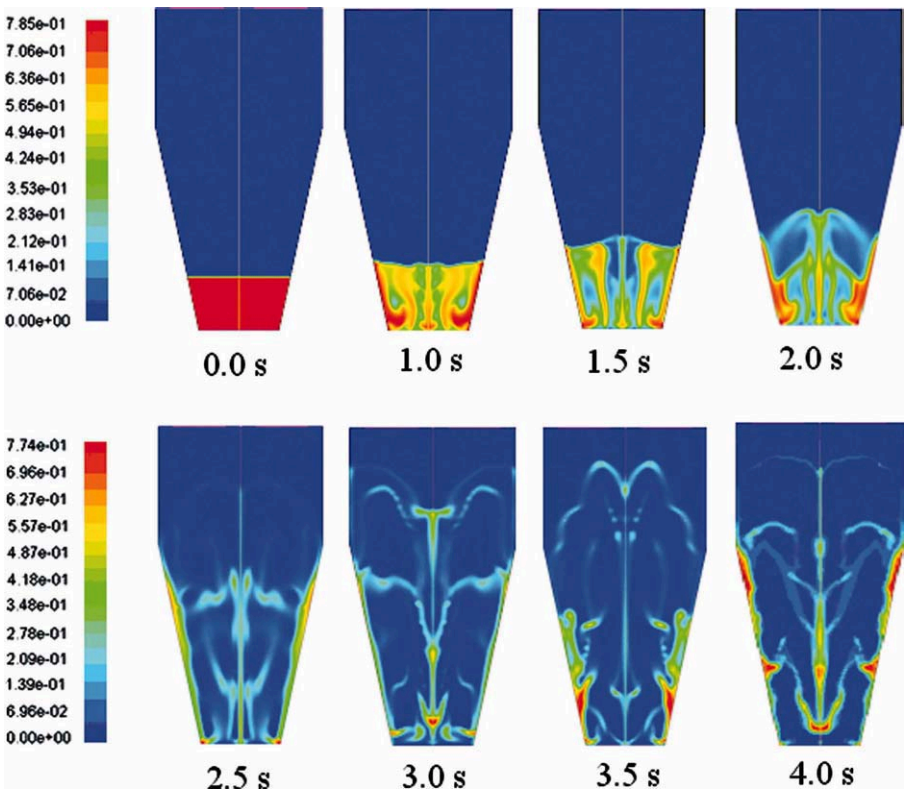

Figure 3. Simulated distribution of solid volume fraction profile for 2D bed (U_g = 1.19 m/s, i.e., ~5U_{mf}, Gidaspow drag model, e_{ss} = 0.9).

[Color figure can be viewed in the online issue, which is available at wileyonlinelibrary.com.]

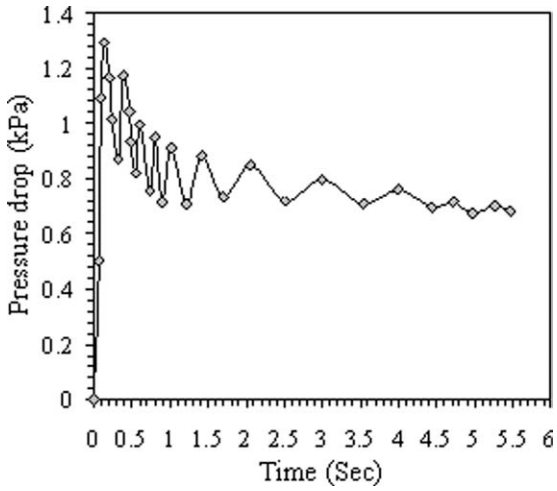

Figure 4. Simulated bed pressure drop using Gidaspow drag model (U_g = 1.19 m/s, e_{ss} = 0.9).

fraction of particles gives way to a gulf-effect with an upward flow in the central region and downward flow near the walls.

Experimental studies have shown that the fluidization behavior of fine particles heavily depends on their properties (e.g., strength, size distribution, and particle type) and on the agglomerates formed during fluidization.[18,51–53] Furthermore, due to the high volume fraction of TiO_2 particles in the annular zone and because they are in contact with each other, TiO_2 agglomerates are formed near the wall. The most common way of fluidizing fine particles is by reducing the granular Bond number, Bo_g, defined as the ratio of interparticle attractive forces (F_o) to particle body forces (F_B) or weight force.[52–54]

$$Bo_g = \frac{F_o}{F_B} \tag{1}$$

When Bo_g number approaches zero the behavior of particles is similar to cohesionless ones, whereas the behavior for high values of this number is similar to sticky particles that are impossible to fluidize.[52] The aspects mentioned clearly show the need for thorough research.

Figure 3 shows a contour plot of solid volume fraction obtained from numerical simulation by using the Gidaspow[55] drag model and partial-slip (φ = 0.5) BC with a gas velocity of 1.19 m/s and static bed height of 0.060 m.

At t = 0.0 s, the bed is in a fixed state, whereas at t = 1.0 s, bed height initially increases with bubble formation and then there is channeling in the center of the bed with gas bubbles passing through this region without forming a spout zone, although the whole bed is fluidized.

At t = 1.5 s, the channels merge and fluidization initially occurs at the central region of the bed. The fluidized region then expands towards the walls. Although this flow pattern is reasonably consistent with our experimental observations, fluidization is delayed in the experimental runs compared to the simulated behavior. The explanation lies in the delayed fluidization near the walls in the experimental runs. Initially, TiO_2 particles tend to stick around the corner of the distributor plate and the gas flow is blocked due to strong binding between the particles and the distributor plate. Subsequently, the volume fraction of particles in the region above the internal spout decreases abruptly, causing a sharp reduction in pressure drop, whereupon the entire bed becomes mobile.

At t = 2.0 s, the formation of the spout zone is observed in the center and annular zone near the walls. After 2.5 s, the gas simply passes through the spout zone, which is established as the path of minimum resistance, causing the fountain to shoot up higher without any significant effect on the overall pressure drop (see also Figure 4). Furthermore, according to the simulation results shown in Figure 4, the overall pressure drop inn the bed peaks with high fluctuations at the beginning of fluidization and then, subsequent ~3.5 s, its value decreases with low fluctuations to around a near steady-state value. Consequently, we use a steady-state model in the simulations and ignore time-averaging terms. Thus, and based on Figures 3 and 4, the simulated pressure drop and bed expansion ratio used for comparing with experimental data are those corresponding to 4.5 s.

Figures 5A–D–7A–D show the solid volume fractions obtained by using the Syamlal-O'Brien,[56] Arastoopour et al.,[57] and Gidaspow[55] drag functions listed in Appendix D, with the partial-slip (φ = 0.5) BC for an initial static bed height or particles loading was 0.048 m,at the superficial gas velocities of 0.3, 0.5, and 1.43 m/s.

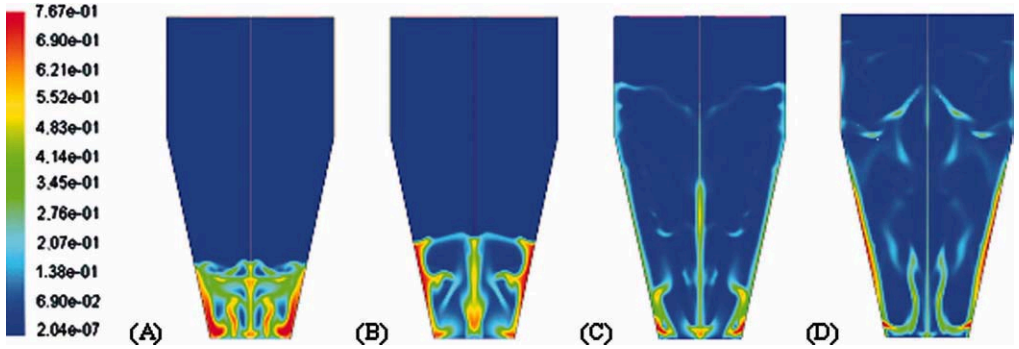

Figure 5. Simulated distribution of solid volume fraction by using Syamlal-O'Brien model.

(A) U_g = 0.3 m/s, e_{ss} = 0.9; (B) U_g = 0.5 m/s, e_{ss} = 0.9; (C) U_g = 1.43 m/s, e_{ss} = 0.9; (D) U_g = 1.43 m/s, e_{ss} = 0.99. [Color figure can be viewed in the online issue, which is available at wileyonlinelibrary.com.]

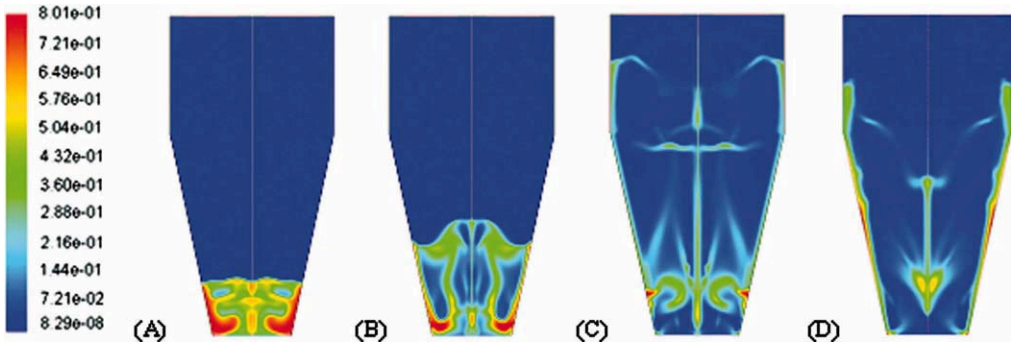

Figure 6. Simulated distribution of solid volume fraction by using Gidaspow model.

(A) $U_g = 0.3$ m/s, $e_{ss} = 0.9$; (B) $U_g = 0.5$ m/s, $e_{ss} = 0.9$; (C) $U_g = 1.43$ m/s, $e_{ss} = 0.9$; (D) $U_g = 1.43$ m/s, $e_{ss} = 0.99$. [Color figure can be viewed in the online issue, which is available at wileyonlinelibrary.com.]

As observed in Figures 5–7, the three drag models predict major changes in the solid volume fraction in both the spout and annular zones with gas velocity. Thus, as gas velocity increased from 0.3 to 1.43 m/s the solid volume fraction decreases in both the spout and annular zones. However, the values of the solid volume fraction in the spout zone are lower than in the annular zone in the full fluidization state.[46] By comparing the flow patterns using different gas velocities, at low gas velocities, i.e., $U_g = 0.3$ m/s (Figures 5–7 A), the bed height initially increases due to bubble formation, and the gas pushes particles back near the inlet, giving way to the formation of a cavity in the packed bed for all models, especially when the Syamlal-O'Brien[56] drag model is used, Figures 5A, B; bed height then decreases and levels off at a steady state. The bubbles become stretched due to bed wall effects and interaction with each other, and then they move upwards, forming larger bubbles. These bubbles burst and split when reaching the top of the bed.

At high gas velocities, i.e., $U_g = 1.43$ m/s, (Figures 5–7 D); large bubble that disrupt the homogeneity of the bed are formed initially, but when the bed reaches steady state, the bubbles disappear and a good particle circulation rate is established, and the three flow regions are observed with the three models.

Nevertheless, according to the literature, it seems that the choice of the drag function and the value of solid volume fraction at different particle loadings may affect the simulated flow patterns and both the over- and under-estimations of the drag models in the particle phase bring about the deviation of the flow pattern from stable fluidization state. Thus, Du et al.[58] showed that the difference between drag models is significant in spouted beds when the solid volume fraction is higher than 0.2, which is the case in these beds, except in the lower section of the spout.

The sensitivity of the bed to the restitution coefficient, e_{ss}, which reflects elastic particle-particle collisions, is investigated in Figures 5C–D–7C–D. As observed, the predictions of the three models are influenced by this parameter.

As observed, an increase in the restitution coefficient from 0.9 to 0.99 leads to the prediction of the bubbling state. Furthermore, an increase in the restitution coefficient involves more elastic particle-particle collisions and particle-phase turbulence and a decrease in the dissipation of granular energy, Eq. A15 (see Appendix A), which leads to large inhomogeneities (or bubbles) in the fluidized bed. The main mechanism for the production of granular energy is the shear caused by the particles falling under gravity near the walls. Consequently, higher solid volume fractions are obtained with a restitution

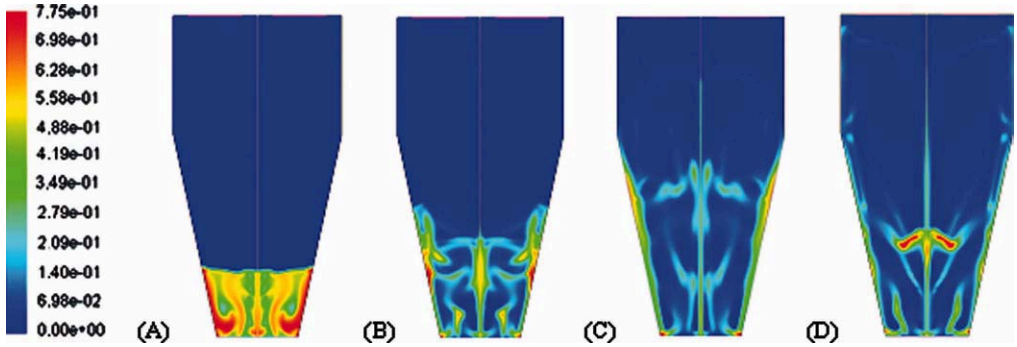

Figure 7. Simulated distribution of solid volume fraction by using Arastoopour model.

(A) $U_g = 0.3$ m/s, $e_{ss} = 0.9$; (B) $U_g = 0.5$ m/s, $e_{ss} = 0.9$; (C) $U_g = 1.43$ m/s, $e_{ss} = 0.9$; (D) $U_g = 1.43$ m/s, $e_{ss} = 0.99$. [Color figure can be viewed in the online issue, which is available at wileyonlinelibrary.com.]

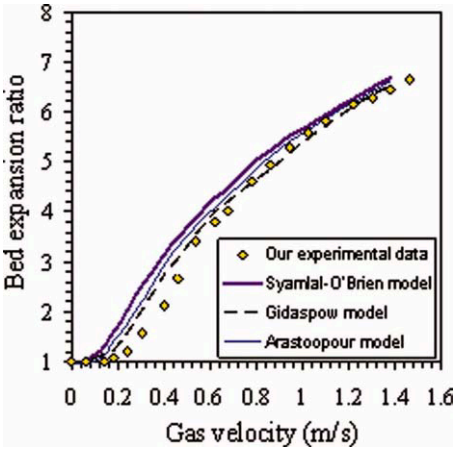

Figure 8. Comparison of experimental and simulated bed expansion ratios.

[Color figure can be viewed in the online issue, which is available at wileyonlinelibrary.com.]

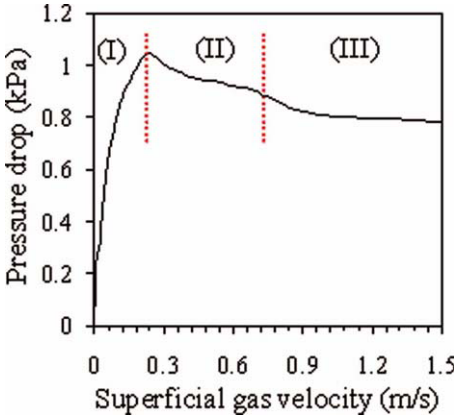

Figure 10. Experimental pressure drop across the bed (H_o = 0.060 m).

[Color figure can be viewed in the online issue, which is available at wileyonlinelibrary.com.]

coefficient of 0.9 than with e_{ss} = 0.99, Figures 5C–D–7C–D. Goldschmidt et al.[59] reported that varying this parameter had a significant impact on bubbling bed hydrodynamics with Geldart B particles, but simulation results obtained by Neri and Gidaspow,[31] McKeen and Pugsley[60] and Almuttahar and Taghipour[38] show that the restitution coefficient plays only a minor role in a multiphase system with Geldart A particles (such as FCC particles) in a circulating fluidized bed riser. Therefore, the value of the restitution coefficient was maintained at 0.9 in subsequent simulations.

The experimental data and simulation results for the bed expansion ratio (H/H_o) using the Syamlal-O'Brien,[56] Arastoopour et al.,[57] and Gidaspow[55] drag functions for a static bed height (H_o) of 0.048 m and several superficial gas velocities are depicted in Figure 8. The three models consistently predict an increase in bed expansion by increasing gas velocity. The relative standard deviation between experimental data and the CFD simulation results for the bed expansion ratio using Syamlal-O'Brien, Arastoopour and Gidaspow are 10.4%, 8.2%, and 6.8%, respectively. Clearly, the Gidaspow drag function is better at predicting bed expansion than the Syamlal-O'Brien and Arastoopour drag functions.

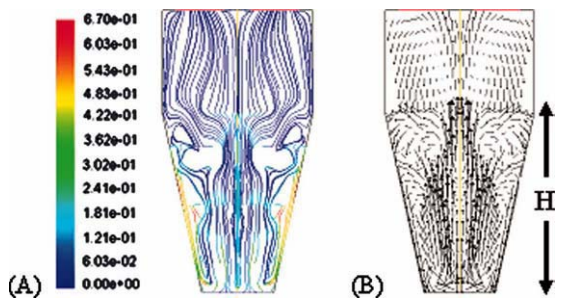

Figure 9. (A) Simulated path lines and (B) Vector velocities of particles.

(H_o = 0.024 m, U_g = 1.19 m/s, drag function: Gidaspow, e_{ss} = 0.9). [Color figure can be viewed in the online issue, which is available at wileyonlinelibrary.com.]

Flow recirculation and, consequently, intense particle mixing are expected with air velocities of 1.19 m/s. Based on the observation of air-solid particle flow, the particle mixing behavior in conical fluidized beds is due to the following three mechanisms: (1) diffusion—particles diffuse from the central spout region to the annular dense region, especially in the middle of the bed. (2) Transportation and circulation—particles are transported upwards in the spout region and then, when they reach the upper part of the bed (section H in Figure 9), move downwards in the dense annular region. Subsequently, particles entrain from the dense annular region into the spout region, especially in the distributor region, leading to continuous circulation and mixing. (3) Bubble action—bubbles containing particles move upwards and outwards, which contributes to their radial and axial mixing. The simulated path lines and particle velocity vectors in the bed are shown in Figures 9A, B, respectively, which have been calculated by using the Gidaspow drag model for a static bed height (H_o) of 0.024 m. Path lines are the lines travelled by neutrally buoyant particles in equilibrium with the fluid motion and are an excellent tool for the visualization of complex two- or three-dimensional flows. The simulation of path lines is presented in Figure 9A. The air bubbled through the bed flows towards the outlet following a recirculation path. Figure 9B also shows the expanded bed obtained by simulation at U_g = 1.19 m/s.

The static-to-fluidized bed transition mechanism is best described by means of a plot of pressure drop as a function of superficial gas velocity. This plot is usually called a characteristic curve.[24,43,61,62] In this curve, pressure drop gradually increases by increasing gas velocity and a point is reached at which pressure drop approximately balances the weight of particles per unit area.

Figure 10 shows the experimental pressure drop across the bed when the static bed height or particle loading is 0.060 m. As observed, as superficial gas velocity is increased above 0.24 m/s, the flow regime changes from fixed bed (I) to core-type partial fluidized bed (II). In this state, pressure drop is above the weight of particles per unit area, which

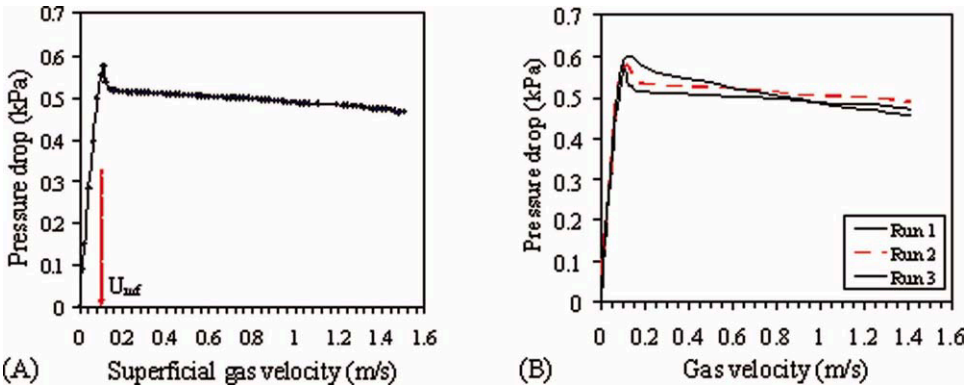

Figure 11. Simulated bed pressure drop using Gidaspow drag model for H_o = 0.012 m.

[Color figure can be viewed in the online issue, which is available at wileyonlinelibrary.com.]

has been termed as overpressure in the fluidization literature.[17,43,53,55,63–66] This overpressure is required to overcome the adhesion between TiO_2 particles and between these particles and the wall. In the case of this system with poly-dispersed TiO_2 particles, overpressure is found to be accompanied by vigorous eruption of particles via local channeling in the bed.

At high superficial velocities above 0.5 m/s, the flow regime changes from core-type to a fully fluidized bed (III) state.

Figures 11–14 show the experimental (Figures 11A–14A) and simulated (Figures 11B–14B) pressure drop values across the bed as a function of superficial gas velocity. The Gidaspow drag function has been used to obtain the simulated values. Four static bed heights, i.e., 0.012, 0.024, 0.048, and 0.060 m, of poly-dispersed TiO_2 particles have been used in the experiments, whereas an average particle diameter equal to 280 μm has been taken for all simulations. The experiments show that at the initial stage of relatively low velocities (below 0.1 m/s) TiO_2 particles tend to stick to each other and to the walls with almost no particle motion. At this stage, the bed is in a fixed state (stretch I in Figure 10), and once a peak pressure drop has been reached fluidization starts abruptly for higher velocities (above 0.7 m/s), but severe channeling takes places at the same time, which gives way to a decrease in pressure drop. The experimental data (Figures 11A–14A) show that pressure drop remains approximately constant around 465, 520, 690, and 785 Pa for the static bed heights of 0.012, 0.024, 0.048, and 0.060 m, respectively. This is an indication that wall friction has a greater influence on the overall pressure drop as particle loading is increased. Figures 11A–14A also show that as static bed height is increased from 0.012 m to 0.024, 0.048, and 0.060 m the peak pressure drop increases from 580 to 690, 940, and 1050 Pa, respectively.

According to Figures 11A–14A and to visual observations, the minimum fluidization velocity, U_{mf}, is that corresponding to the peak pressure drop and it increases as static bed height is increased. Thus, for the static bed heights of 0.012, 0.024, 0.048, and 0.060 m, the minimum fluidization velocities are 0.10 to 0.11, 0.18, and 0.23 m/s, respectively. The increase in the minimum fluidization velocity is due to the fact that the conical vessel containing low static bed heights allows higher superficial gas velocities and flow dissipation rates than high static bed heights.

Figures 11B–14B show that the simulated pressure drop values are lower than the experimental data obtained by increasing gas velocity step by step. The highest deviations

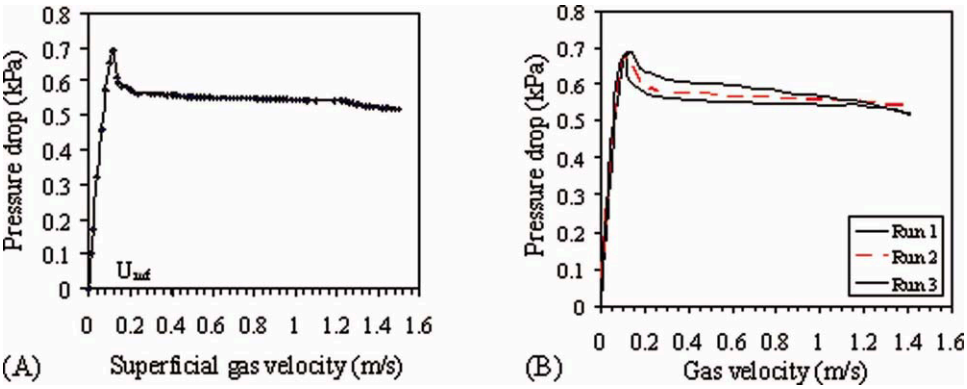

Figure 12. Simulated bed pressure drop using Gidaspow drag model for H_o = 0.024 m.

[Color figure can be viewed in the online issue, which is available at wileyonlinelibrary.com.]

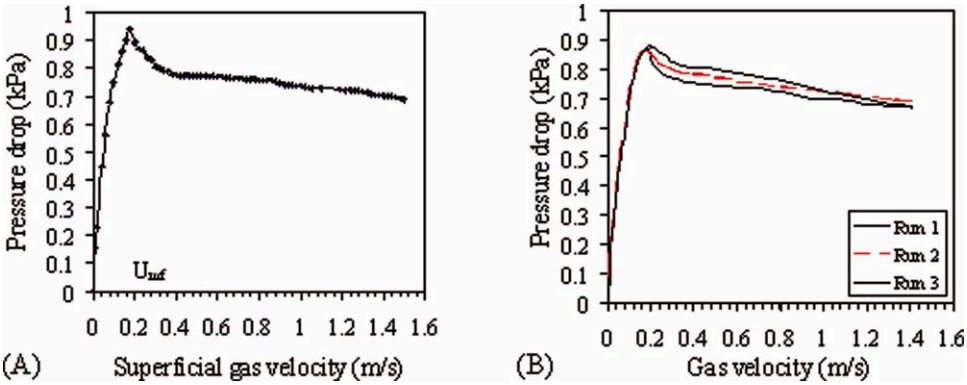

Figure 13. Simulated bed pressure drop using Gidaspow drag model for H_o = 0.048 m.

[Color figure can be viewed in the online issue, which is available at wileyonlinelibrary.com.]

are found at relatively low gas velocities, corresponding to $U \approx 1$–$3U_{mf}$. Therefore, the simulation results show better agreement with the experimental data at velocities above $U \approx 4$–$6U_{mf}$. Under these conditions ($U >> U_{mf}$), the flow of gas and particles is fully developed, there is no acceleration or deceleration of particles and these recirculation at the walls, whereby pressure drop is constant.

Table 4 shows the experimental and simulation results for the minimum fluidization velocity obtained using the three different types of BC for four static bed heights. Table 5 shows the relative deviation between the experimental data and those obtained in the simulation using each type of BC.

According to Figures 11–14 and Tables 4 and 5, the following points should be noted: (1) an increase in the static bed height tends to cause more TiO_2 particle agglomeration due to particle-particle collisions in the bed. Therefore, the highest deviations between the experimental and simulation results are found at the maximum particle loading studied (H_o = 0.060 m). Based on Figure 14A, the two velocities that best describe bed behavior are the incipient fluidization velocity (primary minimum fluidization velocity, U_{mf}) for a superficial gas velocity of 0.236 m/s, and the complete fluidization velocity for a superficial gas velocity ~0.7 m/s (i.e., $U_g \approx 3U_{mf}$). Tanfara et al.[23] studied the mixing and segregation behavior of fluidized beds and defined a diameter ratio, d_R, as the ratio of the mean diameter of the larger particle to the smaller particle. When d_R is between 1 and 2, mixing is complete, whereas for larger values of d_R segregation is significant and excess gas velocities are needed for complete particle mixing. Given that the agglomeration of TiO_2 particles in the bed occurs throughout fluidization, the values of diameter ratio (d_R) have been determined, and they are ~2.5 (~312 μm–125 μm) and 3.2 (~480 μm–150 μm) for particle loadings H_o = 0.012 and H_o = 0.060 m, respectively. This means that further research is required on the minimum fluidization velocity with high particle loadings ($H_o > 0.060$ m).

(2) For low particle loadings (i.e., H_o = 0.012 m), because of its dependency on α_s^2 the main dissipation is due to the drag interaction between gas and particles. Therefore, the lowest value of φ (φ = 0 or zero shear condition at the wall), corresponding to the free-slip BC, is required to obtain reasonable agreement with experimental data.

(3) The determination of the best BC for the model is difficult when the static bed height is 0.024 m, given that the results obtained with the three types of BC are close to each other.

(4) The use of the partial-slip BC (φ = 0.5) in the simulations gives the lowest value of the mean standard deviation compared to the other BC. This is explained by the facts mentioned in points 1 and 2. Thus, the lowest deviations between the experimental data and simulation results are found for low particle loadings and, for these beds, the

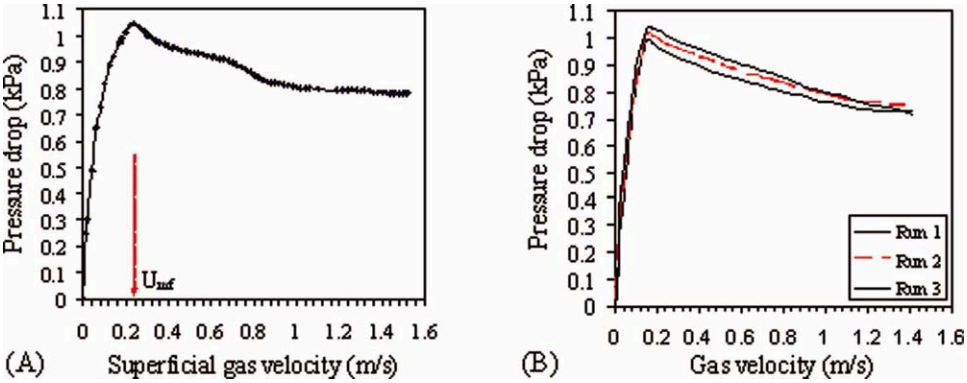

Figure 14. Simulated bed pressure drop using Gidaspow drag model for H_o = 0.060 m.

[Color figure can be viewed in the online issue, which is available at wileyonlinelibrary.com.]

Table 4. Experimental and Simulated Values of Minimum Fluidization Velocity

	U_{mf} (m/s)			
H_o (m)	Exp.	Run 1	Run 2	Run 3
0.012	0.108	0.101	0.103	0.102
0.024	0.117	0.108	0.110	0.109
0.048	0.180	0.161	0.163	0.162
0.060	0.236	0.207	0.211	0.208

Table 5. Relative Standard Deviation Between the Experimental and Simulation Results of Minimum Fluidization Velocity

	Relative Standard Deviation (%)		
H_o (m)	Run 1	Run 2	Run 3
0.012	6.30	4.62	5.75
0.024	7.60	5.98	7.07
0.048	10.55	9.44	10.00
0.060	12.28	10.59	11.86
Mean standard deviation	9.18	7.65	8.84

lowest value of specularity coefficient is required. Furthermore, relevant studies[38,41] shows that steady-state solutions, like those obtained in this study by ignoring the terms arising from time-averaging, require the use of high values of φ. Therefore, introducing the mean value of φ, corresponding to the partial-slip BC instead of free- or no-slip BC, gives way to a slightly better prediction of the minimum fluidization velocity.

Simulated bed expansion bed ratios (H/H_o) are compared in Figure 15 ($H_o = 0.012$ m (Figure 15A) and $H_o = 0.060$ m (Figure 15B) using the Gidaspow[55] drag function and the three BC for two static bed heights.

According to Figure 15, the following points should be noted: (1) bed expansion ratio increases almost linearly by increasing gas velocity. (2) An increase in static bed height from 0.012 to 0.060 m leads to a decrease in bed expansion ratio from a value of about 15.3 to 5.7, respectively, at a superficial gas velocity of 1.4 m/s. This is explained by the fact that, increasing TiO_2 particle loading causes more agglomeration of finer particles ($d_p < 120$ μm) due to interparticle forces, such as van der Walls or electrostatic forces in the absence of moisture force. Kinetic energy is dissipated in the agglomeration process, not only by collision but also by surface cohesion of particle-particle bindings, which may make an even more significant contribution to total energy dissipation.

Table 6 shows the relative standard deviation between the experimental data and the simulation results obtained with the three types of BC. As observed, the simulated bed expansion ratios calculated for low particle loadings (i.e., $H_o = 0.012$ m) using the partial-slip BC (Run 2) and the free-slip BC (Run 3) are similar and more consistent with the experimental data than those calculated using the no-slip BC. In fact, the partial-slip BC (Run 2) was implemented to increase energy dissipation at the wall, which results in a better prediction of the bed expansion ratio. For the higher particle loading ($H_o = 0.060$ m), the fitting is worse for all the simulations, although the results corresponding to the free-slip BC (Run 3) are those that better fit with the experimental data. This result shows that further research is required on the effect of the specularity coefficient in high particle loading systems.

Conclusions

The hydrodynamic behavior of poly-dispersed dried micrometric TiO_2 particles belonging to A/C boundary of Geldart's classification has been studied experimentally and numerically in a conical fluidized bed at different superficial gas velocities and using several static bed heights (particle loadings). The particle flow regime in the conical bed is similar to spouted beds, and there is a transition from the fixed bed to core-type fluidized bed and then to a fully fluidized bed state when the superficial gas velocity is sufficiently high. Similar to spouted beds, three regions are distinguished in the bed, namely, the spout and annular zones in the center and near the walls, respectively, and the fountain located at the top of the bed. The experimental and numerical results show that the bed expansion ratio and pressure drop increase by increasing gas velocity. For low particle loadings (i.e., $H_o = 0.012$ m), the fluidizing gas flows relatively freely through interconnected channels and cracks, and the bed becomes

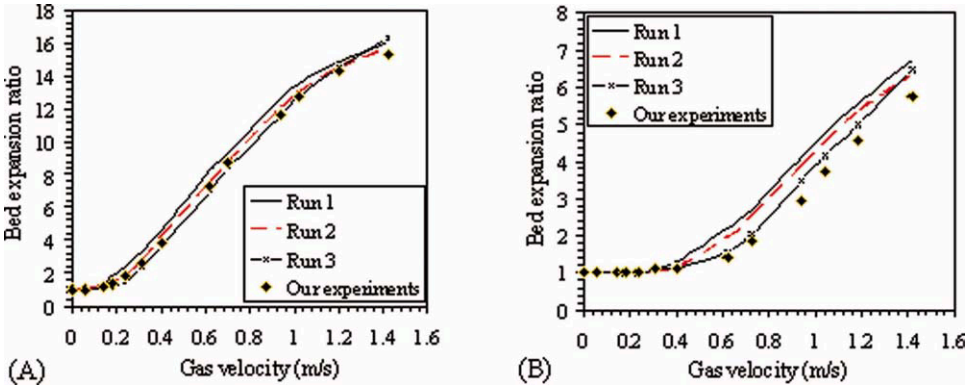

Figure 15. Comparison of experimental data and simulated bed expansion ratios. (A) $H_o = 0.012$ m, (B) $H_o = 0.060$ m.

[Color figure can be viewed in the online issue, which is available at wileyonlinelibrary.com.]

Table 6. Relative Standard Deviation Between the Experiments with the Simulated Bed Expansion Ratio

	Relative Standard Deviation (%)		
H_o (m)	Run 1	Run 2	Run 3
0.012	7.20	3.95	4.12
0.060	12.14	10.10	8.56

fully fluidized when pressure drop overcomes particle weight per unit area, whereas for high particle loadings (i.e., H_o = 0.060 m), fluidization occurs first in the central region of the bed and then extends toward the walls as the superficial gas velocity is gradually increased.

The minimum fluidization velocity is determined for different particle loadings from the relationship between differential bed pressure drop and gas velocity. An increase in bed depth from 0.012 to 0.060 m leads to an increase in minimum fluidization velocity from 0.108 to 0.23 m/s, whereas it leads to a decrease in the bed expansion ratio from 15.3 to 5.7, respectively. For high particle loadings (i.e., H_o = 0.060 m), two velocities (incipient and complete fluidization velocity) are required to describe bed behavior, whereas for low particle loadings (i.e., H_o = 0.012 m), only the minimum fluidization velocity is noted in a characteristic curve.

The Eulerian-Eulerian approach is applied to model gas-solid two-phase flow of TiO_2 micro-sized particles at steady state. The simulations have been run using the Syamlal-O'Brien,[56] Arastoopour et al.,[57] and Gidaspow[55] drag functions, and the results obtained have been compared with the experimental data. The main conclusion is that the drag function proposed by Gidaspow[55] gives a better prediction than the other ones for bed expansion ratio and the Syamlal-O'Brien[54] drag function predicts a bubbling state and lower bed expansion than the other ones. Furthermore, an increase in the restitution coefficient value from 0.9 to 0.99 predicts the bubbling state. The simulation results using the Gidaspow drag function predict the spout, annular and fountain zones that have been experimentally observed. Three different types of BC, i.e., no-slip, free-slip, and partial-slip (φ = 0.5), have been used in the numerical simulation of the solid phase at the vessel wall.

The highest deviations between the experimental data and simulation results in the characteristic curves have been found for high particle loadings (i.e., H_o = 0.060 m), which is explained because increasing particle loading causes more agglomeration of TiO_2 fine particles. These conditions can be minimized or prevented by reducing particle loading. Furthermore, the use of the partial-slip BC (φ = 0.5) in the simulations gives a lower value of mean standard deviation in the determination of the minimum fluidization velocity than when using the free- or no-slip boundary. However, the results obtained for bed expansion ratio using the free-slip BC are slightly better than those obtained by implementing the model with the other BC. A final remark is the need for further experimental and simulation studies with high particle loadings for the validation of CFD models in conical fluidized beds.

Acknowledgments

The authors thank the Hamedan University of Technology and Laser and Optic Research School of Iran for optical experiments and digital analysis and the Spanish Ministry of Science and Education (Project CTQ2007-61167).

Notation

Symbols

B = slip coefficient, dimensionless
Bo_g = granular bond number, dimensionless
C_D = drag coefficient, dimensionless
$C1\mu$, $C1\varepsilon$, $C2\varepsilon$, $C3\varepsilon$ = constants in the gas turbulence model
d_i = inlet diameter, m
d_p = particle diameter, m
$d_{p,\,avg}$ = average particle diameter, m
e_{ss} = Restitution coefficient, dimensionless
g = acceleration due to gravity, m/s^2
$g_{0,ss}$ = radial distribution coefficient, dimensionless
h = total height of column, m
H = expanded bed height, m
H_o = static bed height, m
$\bar{I}$ = Stress tensor, dimensionless
I_{2D} = Second invariant of the strain rate tensor, s^{-2}
k = Turbulent kinetic energy, kg/ms^3
k_g = turbulence quantities of gas phase, m^2/s^2
$k\,\theta_s$ = diffusion coefficient for granular energy, kg/ms
P = Pressure, Pa
p_f = frictional stress, dimensionless
R,r = Radius, m
Re = Reynolds number, dimensionless
T = time, s
U,u = gas velocity, m/s
V = particle velocity, m/s
X = weight fraction
z = height from the bottom of the vessel

Greek letters

α_i = volume fraction, dimensionless
α_i = loose bed volume fraction, dimensionless
β = Momentum interphase exchange coefficient, dimensionless
ε = turbulence dissipation rate, m^2/s^3
$\gamma\theta_m$ = collision dissipation of energy, kg/ms^3
γ = cone angle
ϕ_{gs} = transfer rate of kinetic energy, kg/ms^3
φ = specularity coefficient, dimensionless
θ_i = granular temperature, m^2/s^2
λ_i = bulk viscosity, kg/ms
μ_i = shear viscosity, kg/ms
Π = turbulence exchange terms between gas and solid phases
ν_i = kinematic viscosity, m^2/s
ρ_i = density, kg/m^3
$\bar{\bar{\tau}}_i$ = stress tensor, Pa
$\tau^t_{s,g}$ = Lagrangian integral time scale, s
$\tau^x_{s,g}$ = particle relaxation time, s

Subscripts

b = Bulk
g = gas
i = general index
mf = minimum fluidization
o = outlet
p = particle
q = phase
s = solids
t = terminal (e.g. vt is the terminal velocity)
w = wall

Literature Cited

1. Becker HA, Salans HR. Drying wheat in a spouted bed. *Chem Eng Sci*. 1960;139:97–112.

2. Kmiec A. Hydrodynamics of flow and heat transfer in spouted beds. *Chem Eng J*. 1980;19:189–200.
3. Wormsbecker M, Pugsley T, Tanfara H. Interpretation of the hydrodynamic behavior in a conical fluidized bed dryer. *Chem Eng Sci*. 2009;64:1739–1746.
4. Wormsbecker M, van Ommen R, Nijenhuis J, Tanfara H, Pugsley T. The influence of vessel geometry on fluidized bed dryer hydrodynamics. *Powder Technol*. 2009;194:115–125.
5. Depypere F, Pieters JG, Dewettinck K. Expanded bed height determination in a fluidized bed reactor. *J Food Eng*. 2005;67:353–359.
6. Senadeera W, Wijesinghe B, Young G, Bhandari B. Fluidization characteristics of moist food particles. *Int J Food Eng*. 2006;2:(art. 7).
7. Jono K, Ichikawa H, Miyamoto M, Fukumori Y. A review of particulate design for pharmaceutical powders and their production by spouted bed coating. *Powder Technol*. 2000;113:269–277.
8. Chaplin G, Pugsley T, Winters C. Application of chaos analysis to pressure fluctuation data from a fluidized bed dryer containing pharmaceutical granule. *Powder Technol*. 2004;142:110–120.
9. Wormsbecker M, Adams A, Pugsley T, Winter C. Segregation by size difference in a conical fluidized bed of pharmaceutical granulate. *Powder Technol*. 2005;153:72–80.
10. Pugsley T, Chaplin G, Khanna P. Application of measurement techniques to conical Lab-scale fluidized bed dryers containing pharmaceutical. *Trans IChemE*. 2007;85:273–283.
11. Salam PA, Bhattacharya SC. A comparative study of characoal gasification in two types of spouted bed reactors. *Energy*. 2006;31:228–243.
12. Olazar M, Aguado R, Bilbao J, Barona A. Pyrolysis of sawdust in a conical spouted bed contactor with a HZSM-5 catalyst. *AIChE J*. 2000;46:1025–1033.
13. Olazar M, Lopez G, Arabiourrutia M, Elordi G, Aguado R, Bilbao J. Kinetic modelling of tyre pyrolysis in a conical spouted bed reactor. *J Anal Appl Pyrol*. 2008;81:127–132.
14. Elordi G, Olazar M, Lopez G, Amutio M, Artetxe M, Aguado R, Bilbao J. Catalytic pyrolysis of HDPE in continuous mode over zeolite catalysts in a conical spouted bed reactor. *J Anal Appl Pyrol*. 2009;85:345–351.
15. Bilbao J, Olazar M, Romero A, Arandes JM. Design and operation of a jet spouted bed reactor with continuous catalyst feed in the benzyl alcohol polymerization. *Ind Eng Chem Res*. 1995;26:1297–1304.
16. Olazar M, San Jose MJ, Zabala G, Bilbao J. A new reactor in jet spouted bed regime for catalytic polymerizations. *Chem Eng Sci*. 1994;49:4579–4588.
17. San Jose MJ, Olazar M, Aguado R, Bilbao J. Influence of the conical section geometry on the hydrodynamics of shallow spouted beds. *Chem Eng J*. 1996;62:113–120.
18. Geldart D. Types of gas fluidization. *Powder Technol*. 1973;7:285–292.
19. Geldart D. The effect of particle size and size distribution on the behavior of gas-fluidized beds. *Powder Technol*. 1972;6:201–215.
20. Geldart D. and Rhodes MJ. Survey of current world-wide research in gas fluidization (January 1989–December 1991). *Powder Technol*. 1992;71:1–46.
21. Alavi S, Caussat B, Experimental study on fluidization of micronic powders. *Powder Technol*. 2005;157:114–120.
22. Wang SY, He YR, Lu HL, Zheng JX, Liu GD, Ding YL. Numerical simulations of flow behavior of agglomerates of nano-size particles in bubbling and spouted beds with an agglomerate-based approach. *Trans IChemE Part C*. 2007;85:231–240.
23. Tanfara H, Pugsley T, Winters C. Effect of particle size distribution on local voidage in a bench-scale conical fluidized bed dryer. *Drying Technol*. 2002;20:1273–1289.
24. Mathur KB, Epstein N. *Spouted Beds*. New York: Academic Press, Inc Ltd., 1974:304.
25. Epstein N, Grace JR. *Spouting of particulate solids*. In: Otten L, Fayed ME, editors. *Handbook of Powder Science and Technology*, *Chapter 11*. Van Nostrand Reinhold, 1984.
26. Olazar M, Lopez G, Altzibar H, Barona A, Bilbao J. One-dimensional modelling of conical spouted beds. *Chem Eng Proc* 2009;48:1264–1269.
27. Lefroy GA, Davidson JF. The mechanism of spouted beds. *Trans Inst Chem Eng*. 1969;47:120–128.
28. Littman H, Narayanan PV, Tomlis AH, Friedman ML. A complete theoretical model for a first order isothermal catalytic reaction in a spouted bed. *AIChE Symp Ser*. 1981;77:174–180.
29. Ergun S. Fluid flow through packed columns. *Chem Eng Prog*. 1952;48; 89–94.
30. Kwauk M. Bubbleless fluidization, fluidization. *Solids Handling Process* 1998; 492–581.
31. Neri A, Gidaspow D. Riser hydrodynamics: simulation using kinetic theory. *AIChE J*. 2000;46:52–67.
32. Gidaspow D. Hydrodynamics of fluidization using kinetic theory: an emerging paradigm? *Recent Res Dev Chem Eng Sci*. 2003;5:53–81.
33. Grace J, Taghipour F. Verification and validation of CFD models and dynamic similarity for fluidized beds. *Powder Technol*. 2004;139:99–110.
34. Cooper S, Coronella CJ. CFD simulations of particle mixing in a binary fluidized bed. *Powder Technol*. 2005;151:27–36.
35. Benyahia S, Syamlal M, O'Brien TJ. Evaluation of boundary conditions used to model dilute, turbulent gas/solids flows in a pipe. *Powder Technol*. 2005;156:62–72.
36. Benyahia S, Syamlal M, O'Brien TJ. Study of the ability of multiphase continuum models to predict core-annulus flow. *AIChE J*. 2007;53:2549–2568.
37. Shirvanian PA, Calo JM, Hradil G. Numerical simulation of fluid-particle hydrodynamics in a rectangular spouted vessel. *Int J Multiphase Flow*. 2006;32:739–753.
38. Almuttahar A, Taghipour F. Computational fluid dynamics of high density circulating fluidized bed riser: study of modeling parameters. *Powder Technol*. 2008;185:11–18.
39. Huilin L, Yurong H, Wentie L. Ding J, Gidaspow D, Bouillard J. Computer simulations of gas-solid flow in spouted bed using kinetic-frictional stress model of granular flow. *Chem Eng Sci*. 2004;59:865–878.
40. Darelius A, Rasmuson A, VanWachem B, Bjorn IN, Folestad S. CFD simulation of the high shear mixing process using kinetic theory of granular flow and frictional stress models. *Chem Eng Sci*. 2008;63:2188–2197.
41. Taghipour F, Ellis N, Wong C. Experimental and computational study of gas-solid fluidized bed hydrodynamics. *Chem Eng Sci*. 2005;60:6857–6867.
42. Johnson PC, Jackson R. Frictional-collisional constitutive relations for granular materials, with application to plane shearing. *J Fluid Mech*. 1987;176:67–93.
43. Olazar M, San Jose MJ, Aguayo AT, Arandes JM, Bilbao J. Pressure drop in conical spouted beds. *Chem Eng J*. 1993;51:53–60.
44. He YL, Qin SZ, Lim CJ, Grace JR. Particle velocity profiles and solid flow patterns in spouted beds. *Canad J Chem Eng*. 1994;72:561–568.
45. San Jose MJ, Olazar M, Alvarez S, Morales A, Bilbao J. Local porosity in conical spouted beds consisting of solids of varying density. *Chem Eng Sci*. 2005;60:2017–2025.
46. Bahramian A, Kalbasi M, Olazar M. Influence of boundary conditions on cfd simulation of gas-particle hydrodynamics in a conical fluidized bed unit. *Int J Chem React Eng*. 2009;7:1–27.
47. Syamlal M. *MFIX documentation: numerical techniques, DOE/MC-31346–5824 NTIS/DE98002029*. Springfield, VA: National Technical Information Service. 1998.
48. Benyahia S, Syamlal M, O'Brien TJ. Multiphase flow with interphase eXchanges version MFIX-2010-1 (Date: 02/02/2010). Available at http://www.mfix.org/documentation/Mfix Equations.
49. Schaeffer DG. Instability in the evolution equations describing incompressible granular flow. *J Diff Eq*. 1987;66:19–50.
50. Jung J, Gidaspow D. Fluidization of nano-size particles. *J Nanoparticle Res*. 2002;4:438–497.
51. Wang ZG, Bi HT, Lim J. Numerical simulations of hydrodynamic behavior in conical spouted beds. *China Particulogy*. 2006;4:194–203.
52. Hristov J. Magnetically assisted gas-solid fluidization in a tapered vessel: first report with obeservations and dimensional analysis. *Canad J Chem Eng*. 2008;86:470–492.
53. Wang XS, Rahman F, Rhodes MJ. Nanoparticle fluidization and Geldart's classification. *Chem Eng Sci*. 2007;62:3455–3461.
54. Rhodes MJ, Wang XS, Nguyen M, Stewart P, Liffman K. Onest of cohesive behavior in gas fluidized beds: a numerical study using DEM simulation. *Chem Eng Sci*. 2001;56:4433–4438.
55. Gidaspow D. *Multiphase Flow and Fluidization*, 1st ed. London: Academic Press, 1994.
56. Syamlal M, O'Brien TJ. Computer simulation of bubbles in a fluidized bed. *AIChE Symp Ser*. 1989;85:22.

57. Arastoopour H, Pakdel P, Adewumi M. Hydrodynamics analysis of dilute gas- solid flow in a vertical pipe. *Powder Technol*. 1990;62: 163–170.
58. Du W, Bao X, Xu J, Wei W. Computational fluid dynamics (CFD) modeling of spouted bed: assessment of drag coefficient correlations. *Chem Eng Sci*. 2006;61:1404–1420.
59. Goldschmidt MJV, Kuipers JAM, van Swaaij WPN. Hydrodynamic modeling of dense gas-fluidized beds using the kinetic theory of granular flow: effect of coefficient of restitution on bed hydrodynamics. *Chem Eng Sci*. 2001;72:561–568.
60. McKeen T, Pugsley T. Simulation and experimental validation of a freely bubbling bed of FCC catalyst. *Powder Technol*. 2003;129: 139–152.
61. Duarte CR, Olazar M, Murata VV, Barrozo MAS. Numerical simulation and experimental study of fluid-particle flows in a spouted bed. *Powder Technol*. 2008;188:195–205.
62. Sau DC, Mohanty S, Biswal KC. Critical fluidization velocities and maximum bed pressure drops of homogeneous binary mixture of irregular particles in gas–solid tapered fluidized beds. *Powder Technol*. 2008;186:241–246.
63. Li J, Kuipers JAM. Effect of pressure on gas-solid flow behavior in dense gas-fluidized beds; a discrete particle simulation study. *Powder Technol*. 2002;127:173–184.
64. Olazar M, San Jose MJ, Aguayo AT, Arandes JM, Bilbao J. Stable operation conditions for gas-solid contact regimes in conical spouted beds. *Ind Eng Chem Res*. 1992;31:1784–1791.
65. Olazar M, San Jose MJ, Izquierdo MA, Ortiz de Salazar A, Bilbao J. Effect of operating conditions on solid velocity in the spout, annulus and fountain of spouted beds. *Chem Eng Sci*. 2001;56:3585–3594.
66. Simonin O. Continuum modeling of dispersed two-phase flows, in combustion and turbulence in two-phase flow. *Von Karman Institute of Fluid Dynamics Lecture Ser*. 1996:1–47.
67. Wen CY, Yu YH. A generalised method for predicting minimum fluidization velocity. *AIChE J*. 1966;12:610.
68. Syamlal M, O'Brien TJ. Simulation of granular layer inversion in liquid fluidized beds. *Int. J. Multiphase Flow* 1988;14:473–481.
69. Lu HL, He YR, Gidaspow D, Yang LD. Size segregation of binary mixture of solids in bubbling fluidized beds. *Powder Technol*. 2003;134:86–97.
70. Lu HL, Gidaspow D. Hydrodynamics of binary fluidization in a riser: CFD simulation using two granular temperatures. *Chem. Eng. Sci*. 2003;58:3777–3792.

Appendix A

From the point of view of the force balance, drag force is the accelerating force, which acting on the TiO_2 particles and should approximately balance its buoyant weight that arise from the gravity which is the main decelerating force. It is therefore constructive to compare the cohesion forces in relation to the buoyant weight of single particle.

Table A1. Governing Equations for Gas/Solid Flows

Continuity equation for phase i (i = g for gas and s for solid)

$$\frac{\partial}{\partial t}(\alpha_i \rho_i) + \nabla.(\alpha_i \rho_i \vec{v}_i) = 0 \tag{A1}$$

Momentum conservation equation for gas and solid phase

$$\frac{\partial}{\partial t}(\alpha_g \rho_g \vec{U_g}) + \nabla.(\alpha_g \rho_g \vec{U_g} \vec{U_g}) = -\alpha_g \nabla P + \nabla.\bar{\bar{\tau}}_g - \beta(\vec{U_g} - \vec{v}_s) + \alpha_g \rho_g \vec{g} \tag{A2}$$

$$\frac{\partial}{\partial t}(\alpha_s \rho_s \vec{v}_s) + \nabla.(\alpha_s \rho_s \vec{v}_s \vec{v}_s) = -\alpha_s \nabla P + \nabla.\bar{\bar{\tau}}_s - \nabla P_s + \beta(\vec{U_g} - \vec{v}_s) + \alpha_s \rho_s \vec{g} \tag{A3}$$

Granular temperature conservation for solid phase

$$\frac{3}{2}\left[\frac{\partial}{\partial t}(\alpha_s \rho_s \theta_s) + \nabla.(\alpha_s \rho_s \theta_s \vec{v}_s)\right] = -(P_s \bar{\bar{I}} + \alpha_s \bar{\bar{\tau}}_s) : \nabla.\vec{v}_s - \nabla.(k_{\theta s} \nabla \theta_s) - \gamma \theta_s + \phi_{gs} \tag{A4}$$

Table A2. Constitutive Equations for Momentum

Solid stress-strain tensor

$$\bar{\bar{\tau}} = \mu_s \left(\nabla \vec{v}_s + (\nabla \vec{v}_s)^T\right) + \left(\lambda_s - \frac{2}{3}\mu_s\right) \nabla.\vec{v}_s \tag{A5}$$

Fluid-particle interaction exchange coefficient

$$\beta = (1 - \varphi_{gs}) K_{Ergun} + \varphi_{gs} K_{Wen-Yu} \tag{A6}$$

Ergun[29] equation for dense phase calculation

$$\beta = 150 \frac{\alpha_s^2 \mu_g}{\alpha_g d_s^2} + 1.75 \frac{\alpha_s \rho_g}{d_s} \left|\vec{v}_s - \vec{U}_g\right| \quad \alpha_g \leq 0.8 \tag{A7}$$

Wen and Yu[67] equation for dilute phase calculation

$$\beta = \frac{3}{4} C_D \frac{\alpha_s \alpha_g \rho_g \left|\vec{v}_s - \vec{U}_g\right|}{d_s} . \alpha_g^{-2.65} \qquad \alpha_g \rangle 0.8 \tag{A8}$$

Drag function

$$C_D = \frac{24}{Re_s}\left[1 + 0.15(Re_s)^{0.687}\right] \qquad Re_s \langle 1000 \tag{A9}$$

$$C_D = 0.44 \qquad Re_s \geq 1000 \tag{A10}$$

Relative Reynolds number

$$Re_s = \frac{\rho_g . d_s . \left|\vec{v}_s - \vec{U}_g\right|}{\mu_g} \tag{A11}$$

Solid shear viscosity

$$\mu_s = \mu_{s,\,kinetic} + \mu_{s,\,fr} + \mu_{s,col} \tag{A12}$$

Solid bulk viscosity

$$\lambda_s = \frac{4}{3} \varepsilon_s^2 \rho_s d_s g_{0,ss} (1 + e_{ss}) \sqrt{\frac{\theta_s}{\pi}} \tag{A13}$$

Solid frictional viscosity

$$\mu_f = p_f \sin(\varphi) / 2\sqrt{I_{2D}} \tag{A14}$$

Collision dissipation of energy

$$\gamma \theta_m = \frac{12(1 - e_{ss}^2) g_{0,ss}}{d_p \sqrt{\pi}} \rho_s \alpha_s^2 \theta_s^{3/2} \tag{A15}$$

Solid pressure

$$P_s = \alpha_s \rho_s \theta_s + 2\rho_s (1 + e_{ss}) \alpha_s^2 g_{0,ss} \theta_s \tag{A16}$$

Radial distribution function

$$g_{0,ss} = \left[1 - \left(\frac{\alpha_s}{\alpha_{s,Max}}\right)^{1/3}\right]^{-1} \tag{A17}$$

Mean particle diameter

$$d_p = 1 / \sum \left(x_i / d_{p_i}\right) \tag{A18}$$

Density of the mixture

$$\rho_p = \sum x_i \rho_i \tag{A19}$$

Granular energy diffusion coefficient

$$K\theta_s = \frac{150 . \rho_s \sqrt{\theta_s . \pi}}{384 . (1 + e_{ss}) . g_{0,ss}} . \left[1 + \frac{6}{5} . \alpha_s . g_{0,ss} . (1 + e_{ss})\right]^2 \tag{A20}$$

Transfer of kinetic energy

$$\phi_{gs} = -3\beta\theta_s \tag{A21}$$

Appendix B

A turbulence model is a computational procedure to close the set of mean flow equations. The choice of turbulence model depends on considerations such as the physically encompassed inlet flow, the established particle for a specific

Table B1. k-ε Turbulence Model, Constants and Parameters

Turbulence kinetic energy (k)

$$\alpha_g\rho_g\left[\frac{\partial k}{\partial t}+\vec{U}_{g,j}\frac{\partial k}{\partial x_j}\right]=\frac{\partial}{\partial x_i}\left(\alpha_g\frac{\mu_{t,g}}{\sigma_k}\frac{\partial k}{\partial x_i}\right)+\alpha_g\tau_{g,ij}\frac{\partial \vec{U}_{g,i}}{\partial x_j}-\alpha_g\rho_g\varepsilon_g+\Pi_{k,g} \tag{B1}$$

Turbulence dissipation rate (ε)

$$\alpha_g\rho_g\left[\frac{\partial \varepsilon}{\partial t}+\vec{U}_{g,j}\frac{\partial \varepsilon}{\partial x_j}\right]=\frac{\partial}{\partial x_i}\left(\alpha_g\frac{\mu_{t,g}}{\sigma_\varepsilon}\frac{\partial \varepsilon}{\partial x_i}\right)+\alpha_g\frac{\varepsilon}{k}\left(C_1\tau_{g,ij}\frac{\partial \vec{U}_{g,i}}{\partial x_j}-C_2\rho_g\varepsilon\right)+\Pi_{\varepsilon,g} \tag{B2}$$

where σ_k and σ_ε are the turbulence Prandtl number for k and ε, respectively

Gas phase stress term

$$\tau_{g,ij}=2\mu_{e,g}.S_{g,ij}\qquad S_{g,ij}=\frac{1}{2}\left(\frac{\partial \vec{U}_{g,i}}{\partial x_j}+\frac{\partial \vec{U}_{g,j}}{\partial x_i}\right)-\frac{1}{3}\frac{\partial \vec{U}_{g,i}}{\partial x_i}\delta_{ij} \tag{B3}$$

Gas phase viscosity model

$$\mu_{e,g}=\min\left(\mu_{max},\mu_g+\mu_{t,g}\right) \tag{B4}$$

For k-ε or Simonin[66] model

$$\mu_{t,g}=\rho_g C_\mu\frac{k_g^2}{\varepsilon} \tag{B5}$$

Turbulence interaction terms for Simonin[66] model

$$\Pi_{k,g}=\beta\left(k_{g,s}-2k_g\right) \tag{B6}$$

$$\Pi_{\varepsilon,g}=C_{3\varepsilon}(\varepsilon/K)\Pi_{k,g} \tag{B7}$$

$$k_{g,s}=\frac{\eta_t}{1+\left(1+X_{s,g}\right)\eta_t}\left(2k+3X_{s,g}\theta_s\right) \tag{B8}$$

Lagrangian integral time scale

$$\tau_{s,g}^t=\frac{\tau_g^t}{\sqrt{1+C_\beta\xi_r^2}} \tag{B9}$$

Time scale of turbulent eddies

$$\tau_g^t=\frac{3}{2}C_\mu\frac{k}{\varepsilon} \tag{B10}$$

Particle relaxation time

$$\tau_{s,g}^x=\frac{\alpha_s\rho_s}{\beta} \tag{B11}$$

Ratio between the Lagrangian integral time scale and the particle relaxation time:

$$\eta_t=\frac{\tau_{s,g}^t}{\tau_{s,g}^x} \tag{B12}$$

New time scale in Simonin model

$$\frac{1}{\tau_s}=\frac{2}{\tau_{g,s}^x}+\frac{\sigma_\xi}{\tau_s^c} \tag{B13}$$

Collisional time scale

$$\tau_s^c=\frac{d_p}{6\alpha_s g_0\sqrt{16\theta_s/\pi}} \tag{B14}$$

Constants in k-ε turbulence model

$$\sigma_k,\sigma_\varepsilon,\ C_\mu,C_{1\varepsilon},C_{2\varepsilon},C_{3\varepsilon}=1.0,\ 1.3,\ 0.09,\ 1.44,\ 1.92,\text{ and }1.22,\ \text{respectively.} \tag{B15}$$

Additional parameters used in turbulence models

$$\xi_r^2=\frac{3\,v_{Slip}^2}{2k},\quad \sigma_c=(1+e)(3-e)/5,\quad x_{s,g}=\frac{\alpha_s\rho_s}{\alpha_g\rho_g},\quad c_\beta=1.8-1.35\cos^2\theta \tag{B16}$$

Here θ is the angle between the mean particle velocity and the mean slip velocity

type of problem, the level of accuracy required, the available computational resources and the amount of time available for the simulation. Turbulence predictions are obtained from the k-ε turbulence model. This model is a semiempirical one based on model transport equations for turbulence kinetic energy (k) and dissipation rate (ε). The model transport equation for k is derived from the exact equation, while the model transport equation for ε is obtained using physical reasoning and bears little resemblance to a mathematically exact counterpart. This model is valid only for fully turbulent flows, and the effects of molecular viscosity are negligible.

Appendix C

The specularity coefficient φ is a measure of the fraction of collisions which transfer momentum to wall and varies from zero (free-slip condition) to one (no-slip condition).

Table C1. Johnson and Jackson[42] Semiempirical Equations

Tangential velocity

$$v_{s,w}=-B\frac{\partial v_{s,w}}{\partial n} \tag{C1}$$

Slip coefficient

$$B=\frac{6\alpha_s.\mu_s}{\sqrt{3}\sqrt{\theta}.\pi.\varphi.\rho_s g_{0,ss}} \tag{C2}$$

Granular temperature at walls,

$$\theta_w=-C_1\frac{\partial\theta_w}{\partial n}+C_2 \tag{C3}$$

Constants

$$C_1=\frac{k\theta_s}{\gamma_w};\quad C_2=\frac{\sqrt{3}\pi\rho_s u_{s,slip}^2 g_{0,ss}\theta_s^{3/2}}{6\alpha_{s,max}} \tag{C4}$$

where

$$\gamma_w=\frac{\sqrt{3}\pi\left(1-e_w^2\right)\alpha_s.g_{0,ss}.\theta_s^{3/2}}{4\alpha_{s,max}} \tag{C5}$$

Appendix D

The drag models and the corresponding correlations of β to be investigated in this study are summarized in Table.

Table D1. Drag Models

Syamlal-O′Brien[68]

$$\beta = \frac{3}{4}\frac{C_D}{f^2}\frac{\rho_g|\bar{v}-u|}{d_P}\alpha_s\alpha_g \tag{D1}$$

where f is the ratio of the solid velocity to the terminal velocity of a single particle.

Arastoopour et al.[57]

$$\beta = \left[\frac{17.3}{Re_P} + 0.336\right]\frac{\rho_g}{d_P}|\bar{v}-u|\alpha_s\alpha_g^{-2.8} \qquad Re_P = \frac{d_P|\bar{v}-u|\rho_g}{\mu_g} \tag{D2}$$

Gidaspow[55]

$$\begin{cases} \beta_{Ergum} = 150\dfrac{\alpha_s^2\mu_g}{\alpha_g d_P^2} + 1.75\dfrac{\alpha_s\rho_g}{d_P}|V-U|, & \alpha_g < 0.8 \\ \beta_{Wen-Yu} = \dfrac{3}{4}C_D\dfrac{\alpha_s\rho_g}{d}|V-U|\alpha_g^{-2.65}, & \alpha_g \geq 0.8 \end{cases} \tag{D3}$$

$$\begin{cases} C_D = \dfrac{24}{Re_{P1}}[1 + 0.15(Re_{P1})^{0.687}], & Re_p < 1000 \\ C_D = 0.44, & {}_p \geq 1000 \end{cases}$$

(*Continued*)

Table D1. (Continued)

$$Re_p = \frac{\alpha_g\rho_g|\bar{v}-u|d_P}{\mu_g}$$

To avoid discontinuity of the two equations, a switch function is introduced to give a rapid transition from refs. 69–70

$$\varphi_{gs} = \frac{\arctan[150\times 1.75(0.2-\alpha_s)]}{\pi} + 0.5$$

$$C_D = \left(0.63 + \frac{4.8}{\sqrt{Re_p/\alpha_s}}\right)^2$$

$$2f = A - 0.06\,Re_P + \sqrt{0.0036\,Re_P^2 + 0.12\,Re_P(2B-A) + A^2}$$

$$A = \alpha_g^{4.14}$$

$$\begin{cases} B = \alpha_g^{2.65}, & \alpha_s < 0.15 \\ B = 0.8\alpha_g^{1.28}, & \alpha_s \geq 0.15 \end{cases}$$

Manuscript received July 31, 2010, revision received Nov. 15, 2010, and final revision received Mar. 14, 2011.